Observation of the Dalitz Decay $\eta' \to \gamma e^+ e^-$

M. Ablikim[1], M. N. Achasov[9,a], X. C. Ai[1], O. Albayrak[5], M. Albrecht[4], D. J. Ambrose[44], A. Amoroso[48A,48C], F. F. An[1], Q. An[45], J. Z. Bai[1], R. Baldini Ferroli[20A], Y. Ban[31], D. W. Bennett[19], J. V. Bennett[5], M. Bertani[20A], D. Bettoni[21A], J. M. Bian[43], F. Bianchi[48A,48C], E. Boger[23,h], O. Bondarenko[25], I. Boyko[23], R. A. Briere[5], H. Cai[50], X. Cai[1], O. Cakir[40A,b], A. Calcaterra[20A], G. F. Cao[1], S. A. Cetin[40B], J. F. Chang[1], G. Chelkov[23,c], G. Chen[1], H. S. Chen[1], H. Y. Chen[2], J. C. Chen[1], M. L. Chen[1], S. J. Chen[29], X. Chen[1], X. R. Chen[26], Y. B. Chen[1], H. P. Cheng[17], X. K. Chu[31], G. Cibinetto[21A], D. Cronin-Hennessy[43], H. L. Dai[1], J. P. Dai[34], A. Dbeyssi[14], D. Dedovich[23], Z. Y. Deng[1], A. Denig[22], I. Denysenko[23], M. Destefanis[48A,48C], F. De Mori[48A,48C], Y. Ding[27], C. Dong[30], J. Dong[1], L. Y. Dong[1], M. Y. Dong[1], S. X. Du[52], P. F. Duan[1], J. Z. Fan[39], J. Fang[1], S. S. Fang[1], X. Fang[45], Y. Fang[1], L. Fava[48B,48C], F. Feldbauer[22], G. Felici[20A], C. Q. Feng[45], E. Fioravanti[21A], M. Fritsch[14,22], C. D. Fu[1], Q. Gao[1], X. Y. Gao[2], Y. Gao[39], Z. Gao[45], I. Garzia[21A], C. Geng[45], K. Goetzen[10], W. X. Gong[1], W. Gradl[22], M. Greco[48A,48C], M. H. Gu[1], Y. T. Gu[12], Y. H. Guan[1], A. Q. Guo[1], L. B. Guo[28], Y. Guo[1], Y. P. Guo[22], Z. Haddadi[25], A. Hafner[22], S. Han[50], Y. L. Han[1], X. Q. Hao[15], F. A. Harris[42], K. L. He[1], Z. Y. He[30], T. Held[4], Y. K. Heng[1], Z. L. Hou[1], C. Hu[28], H. M. Hu[1], J. F. Hu[48A,48C], T. Hu[1], Y. Hu[1], G. M. Huang[6], G. S. Huang[45], H. P. Huang[50], J. S. Huang[15], X. T. Huang[33], Y. Huang[29], T. Hussain[47], Q. Ji[1], Q. P. Ji[30], X. B. Ji[1], X. L. Ji[1], L. L. Jiang[1], L. W. Jiang[50], X. S. Jiang[1], J. B. Jiao[33], Z. Jiao[17], D. P. Jin[1], S. Jin[1], T. Johansson[49], A. Julin[43], N. Kalantar-Nayestanaki[25], X. L. Kang[1], X. S. Kang[30], M. Kavatsyuk[25], B. C. Ke[5], R. Kliemt[14], B. Kloss[22], O. B. Kolcu[40B,d], B. Kopf[4], M. Kornicer[42], W. Kühn[24], A. Kupsc[49], W. Lai[1], J. S. Lange[24], M. Lara[19], P. Larin[14], C. Leng[48C], C. H. Li[1], Cheng Li[45], D. M. Li[52], F. Li[1], G. Li[1], H. B. Li[1], J. C. Li[1], Jin Li[32], K. Li[13], K. Li[33], Lei Li[3], P. R. Li[41], T. Li[33], W. D. Li[1], W. G. Li[1], X. L. Li[33], X. M. Li[12], X. N. Li[1], X. Q. Li[30], Z. B. Li[38], H. Liang[45], Y. F. Liang[36], Y. T. Liang[24], G. R. Liao[11], D. X. Lin[14], B. J. Liu[1], C. X. Liu[1], F. H. Liu[35], Fang Liu[1], Feng Liu[6], H. B. Liu[12], H. H. Liu[1], H. H. Liu[16], H. M. Liu[1], J. Liu[1], J. P. Liu[50], J. Y. Liu[1], K. Liu[39], K. Y. Liu[27], L. D. Liu[31], P. L. Liu[1], Q. Liu[41], S. B. Liu[45], X. Liu[26], X. X. Liu[41], Y. B. Liu[30], Z. A. Liu[1], Zhiqiang Liu[1], Zhiqing Liu[22], H. Loehner[25], X. C. Lou[1,e], H. J. Lu[17], J. G. Lu[1], R. Q. Lu[18], Y. Lu[1], Y. P. Lu[1], C. L. Luo[28], M. X. Luo[51], T. Luo[42], X. L. Luo[1], M. Lv[1], X. R. Lyu[41], F. C. Ma[27], H. L. Ma[1], L. L. Ma[33], Q. M. Ma[1], S. Ma[1], T. Ma[1], X. N. Ma[30], X. Y. Ma[1], F. E. Maas[14], M. Maggiora[48A,48C], Q. A. Malik[47], Y. J. Mao[31], Z. P. Mao[1], S. Marcello[48A,48C], J. G. Messchendorp[25], J. Min[1], T. J. Min[1], R. E. Mitchell[19], X. H. Mo[1], Y. J. Mo[6], C. Morales Morales[14], K. Moriya[19], N. Yu. Muchnoi[9,a], H. Muramatsu[43], Y. Nefedov[23], F. Nerling[14], I. B. Nikolaev[9,a], Z. Ning[1], S. Nisar[8], S. L. Niu[1], X. Y. Niu[1], S. L. Olsen[32], Q. Ouyang[1], S. Pacetti[20B], P. Patteri[20A], M. Pelizaeus[4], H. P. Peng[45], K. Peters[10], J. Pettersson[49], J. L. Ping[28], R. G. Ping[1], R. Poling[43], Y. N. Pu[18], M. Qi[29], S. Qian[1], C. F. Qiao[41], L. Q. Qin[33], N. Qin[50], X. S. Qin[1], Y. Qin[31], Z. H. Qin[1], J. F. Qiu[1], K. H. Rashid[47], C. F. Redmer[22], H. L. Ren[18], M. Ripka[22], G. Rong[1], X. D. Ruan[12], V. Santoro[21A], A. Sarantsev[23,f], M. Savrié[21B], K. Schoenning[49], S. Schumann[22], W. Shan[31], M. Shao[45], C. P. Shen[2], P. X. Shen[30], X. Y. Shen[1], H. Y. Sheng[1], W. M. Song[1], X. Y. Song[1], S. Sosio[48A,48C], S. Spataro[48A,48C], G. X. Sun[1], J. F. Sun[15], S. S. Sun[1], Y. J. Sun[45], Y. Z. Sun[1], Z. J. Sun[1], Z. T. Sun[19], C. J. Tang[36], X. Tang[1], I. Tapan[40C], E. H. Thorndike[44], M. Tiemens[25], D. Toth[43], M. Ullrich[24], I. Uman[40B], G. S. Varner[42], B. Wang[30], B. L. Wang[41], D. Wang[31], D. Y. Wang[31], K. Wang[1], L. L. Wang[1], L. S. Wang[1], M. Wang[33], P. Wang[1], P. L. Wang[1], Q. J. Wang[1], S. G. Wang[31], W. Wang[1], X. F. Wang[39], Y. D. Wang[20A], Y. F. Wang[1], Y. Q. Wang[22], Z. Wang[1], Z. G. Wang[1], Z. H. Wang[45], Z. Y. Wang[1], T. Weber[22], D. H. Wei[11], J. B. Wei[31], P. Weidenkaff[22], S. P. Wen[1], U. Wiedner[4], M. Wolke[49], L. H. Wu[1], Z. Wu[1], L. G. Xia[39], Y. Xia[18], D. Xiao[1], Z. J. Xiao[28], Y. G. Xie[1], Q. L. Xiu[1], G. F. Xu[1], L. Xu[1], Q. J. Xu[13], Q. N. Xu[41], X. P. Xu[37], L. Yan[45], W. B. Yan[45], W. C. Yan[45], Y. H. Yan[18], H. X. Yang[1], L. Yang[50], Y. Yang[6], Y. X. Yang[11], H. Ye[1], M. Ye[1], M. H. Ye[7], J. H. Yin[1], B. X. Yu[1], C. X. Yu[30], H. W. Yu[31], J. S. Yu[26], C. Z. Yuan[1], W. L. Yuan[29], Y. Yuan[1], A. Yuncu[40B,g], A. A. Zafar[47], A. Zallo[20A], Y. Zeng[18], B. X. Zhang[1], B. Y. Zhang[1], C. Zhang[29], C. C. Zhang[1], D. H. Zhang[1], H. H. Zhang[38], H. Y. Zhang[1], J. J. Zhang[1], J. L. Zhang[1], J. Q. Zhang[1], J. W. Zhang[1], J. Y. Zhang[1], J. Z. Zhang[1], K. Zhang[1], L. Zhang[1], S. H. Zhang[1], X. Y. Zhang[33], Y. Zhang[1], Y. H. Zhang[1], Y. T. Zhang[45], Z. H. Zhang[6], Z. P. Zhang[45], Z. Y. Zhang[50], G. Zhao[1], J. W. Zhao[1], J. Y. Zhao[1], J. Z. Zhao[1], Lei Zhao[45], Ling Zhao[1], M. G. Zhao[30], Q. Zhao[1], Q. W. Zhao[1], S. J. Zhao[52], T. C. Zhao[1], Y. B. Zhao[1], Z. G. Zhao[45], A. Zhemchugov[23,h], B. Zheng[46], J. P. Zheng[1], W. J. Zheng[33], Y. H. Zheng[41], B. Zhong[28], L. Zhou[1], Li Zhou[30], X. Zhou[50], X. K. Zhou[45], X. R. Zhou[45], X. Y. Zhou[1], K. Zhu[1], K. J. Zhu[1], S. Zhu[1], X. L. Zhu[39], Y. C. Zhu[45], Y. S. Zhu[1], Z. A. Zhu[1], J. Zhuang[1], L. Zotti[48A,48C], B. S. Zou[1], J. H. Zou[1]

(BESIII Collaboration)

[1] *Institute of High Energy Physics, Beijing 100049, People's Republic of China*
[2] *Beihang University, Beijing 100191, People's Republic of China*
[3] *Beijing Institute of Petrochemical Technology, Beijing 102617, People's Republic of China*
[4] *Bochum Ruhr-University, D-44780 Bochum, Germany*
[5] *Carnegie Mellon University, Pittsburgh, Pennsylvania 15213, USA*
[6] *Central China Normal University, Wuhan 430079, People's Republic of China*
[7] *China Center of Advanced Science and Technology, Beijing 100190, People's Republic of China*
[8] *COMSATS Institute of Information Technology, Lahore, Defence Road, Off Raiwind Road, 54000 Lahore, Pakistan*
[9] *G.I. Budker Institute of Nuclear Physics SB RAS (BINP), Novosibirsk 630090, Russia*
[10] *GSI Helmholtzcentre for Heavy Ion Research GmbH, D-64291 Darmstadt, Germany*
[11] *Guangxi Normal University, Guilin 541004, People's Republic of China*
[12] *GuangXi University, Nanning 530004, People's Republic of China*
[13] *Hangzhou Normal University, Hangzhou 310036, People's Republic of China*

[14] *Helmholtz Institute Mainz, Johann-Joachim-Becher-Weg 45, D-55099 Mainz, Germany*
[15] *Henan Normal University, Xinxiang 453007, People's Republic of China*
[16] *Henan University of Science and Technology, Luoyang 471003, People's Republic of China*
[17] *Huangshan College, Huangshan 245000, People's Republic of China*
[18] *Hunan University, Changsha 410082, People's Republic of China*
[19] *Indiana University, Bloomington, Indiana 47405, USA*
[20] *(A)INFN Laboratori Nazionali di Frascati, I-00044, Frascati, Italy; (B)INFN and University of Perugia, I-06100, Perugia, Italy*
[21] *(A)INFN Sezione di Ferrara, I-44122, Ferrara, Italy; (B)University of Ferrara, I-44122, Ferrara, Italy*
[22] *Johannes Gutenberg University of Mainz, Johann-Joachim-Becher-Weg 45, D-55099 Mainz, Germany*
[23] *Joint Institute for Nuclear Research, 141980 Dubna, Moscow region, Russia*
[24] *Justus Liebig University Giessen, II. Physikalisches Institut, Heinrich-Buff-Ring 16, D-35392 Giessen, Germany*
[25] *KVI-CART, University of Groningen, NL-9747 AA Groningen, The Netherlands*
[26] *Lanzhou University, Lanzhou 730000, People's Republic of China*
[27] *Liaoning University, Shenyang 110036, People's Republic of China*
[28] *Nanjing Normal University, Nanjing 210023, People's Republic of China*
[29] *Nanjing University, Nanjing 210093, People's Republic of China*
[30] *Nankai University, Tianjin 300071, People's Republic of China*
[31] *Peking University, Beijing 100871, People's Republic of China*
[32] *Seoul National University, Seoul, 151-747 Korea*
[33] *Shandong University, Jinan 250100, People's Republic of China*
[34] *Shanghai Jiao Tong University, Shanghai 200240, People's Republic of China*
[35] *Shanxi University, Taiyuan 030006, People's Republic of China*
[36] *Sichuan University, Chengdu 610064, People's Republic of China*
[37] *Soochow University, Suzhou 215006, People's Republic of China*
[38] *Sun Yat-Sen University, Guangzhou 510275, People's Republic of China*
[39] *Tsinghua University, Beijing 100084, People's Republic of China*
[40] *(A)Istanbul Aydin University, 34295 Sefakoy, Istanbul, Turkey; (B)Dogus University, 34722 Istanbul, Turkey; (C)Uludag University, 16059 Bursa, Turkey*
[41] *University of Chinese Academy of Sciences, Beijing 100049, People's Republic of China*
[42] *University of Hawaii, Honolulu, Hawaii 96822, USA*
[43] *University of Minnesota, Minneapolis, Minnesota 55455, USA*
[44] *University of Rochester, Rochester, New York 14627, USA*
[45] *University of Science and Technology of China, Hefei 230026, People's Republic of China*
[46] *University of South China, Hengyang 421001, People's Republic of China*
[47] *University of the Punjab, Lahore-54590, Pakistan*
[48] *(A)University of Turin, I-10125, Turin, Italy; (B)University of Eastern Piedmont, I-15121, Alessandria, Italy; (C)INFN, I-10125, Turin, Italy*
[49] *Uppsala University, Box 516, SE-75120 Uppsala, Sweden*
[50] *Wuhan University, Wuhan 430072, People's Republic of China*
[51] *Zhejiang University, Hangzhou 310027, People's Republic of China*
[52] *Zhengzhou University, Zhengzhou 450001, People's Republic of China*

[a] *Also at the Novosibirsk State University, Novosibirsk, 630090, Russia*
[b] *Also at Ankara University, 06100 Tandogan, Ankara, Turkey*
[c] *Also at the Moscow Institute of Physics and Technology, Moscow 141700, Russia and at the Functional Electronics Laboratory, Tomsk State University, Tomsk, 634050, Russia*
[d] *Currently at Istanbul Arel University, 34295 Istanbul, Turkey*
[e] *Also at University of Texas at Dallas, Richardson, Texas 75083, USA*
[f] *Also at the NRC "Kurchatov Institute", PNPI, 188300, Gatchina, Russia*
[g] *Also at Bogazici University, 34342 Istanbul, Turkey*
[h] *Also at the Moscow Institute of Physics and Technology, Moscow 141700, Russia*

We report the first observation of the Dalitz decay $\eta' \to \gamma e^+e^-$, based on a data sample of 1.31 billion J/ψ events collected with the BESIII detector. The η' mesons are produced via the $J/\psi \to \gamma\eta'$ decay process. The ratio $\Gamma(\eta' \to \gamma e^+e^-)/\Gamma(\eta' \to \gamma\gamma)$ is measured to be $(2.13 \pm 0.09(\text{stat.}) \pm 0.07(\text{sys.})) \times 10^{-2}$. This corresponds to a branching fraction $\mathcal{B}(\eta' \to \gamma e^+e^-) = (4.69 \pm 0.20(\text{stat.}) \pm 0.23(\text{sys.})) \times 10^{-4}$. The transition form factor is extracted and different expressions are compared to the measured dependence on the e^+e^- invariant mass. The results are consistent with the prediction of the Vector Meson Dominance model.

PACS numbers: 13.40.Gp, 14.40.Be, 13.20.Gd, 13.40.Hq

I. INTRODUCTION

Electromagnetic (EM) Dalitz decays of light pseudoscalar mesons, $P \to \gamma l^+ l^-$ ($P = \pi^0$, η, η'; $l = e, \mu$), play an important role in revealing the structure of hadrons and the interaction mechanism between photons and hadrons [1]. If one assumes point-like particles, the decay rates can be exactly calculated by Quantum Electrodynamics (QED) [2]. Modifications to the QED decay rate due to the inner structure of the mesons are encoded in the transition form factor (TFF) $F(q^2)$, where q is the momentum transferred to the lepton pair, and q^2 is the square of the invariant mass of the lepton pair. A recent summary and discussion of this subject can be found in Ref. [3].

The knowledge of the TFF is also important in studies of the muon anomalous magnetic moment, $a_\mu = (g_\mu - 2)/2$, which is the most precise low-energy test of the Standard Model (SM) and an important probe for new physics. The theoretical uncertainty on the SM calculation of a_μ is dominated by hadronic corrections and therefore limited by the accuracy of their determination [4]. In particular, the hadronic light-by-light (HLbL) scattering contribution to a_μ includes two meson-photon-photon vertices that can be related to the form factors in $P \to \gamma\gamma^* \to \gamma e^+ e^-$ decays [4]. Thus, models describing these transitions should be tested as precisely as possible to reduce the uncertainty in the SM prediction for $(g_\mu - 2)/2$.

In this work, the Dalitz decay $\eta' \to \gamma e^+ e^-$ is measured for the first time. The differential decay width, normalized to the radiative decay width $\eta' \to \gamma\gamma$, is [1]

$$\begin{aligned}\frac{d\Gamma(\eta' \to \gamma l^+ l^-)}{dq^2 \Gamma(\eta' \to \gamma\gamma)} &= \frac{2\alpha}{3\pi}\frac{1}{q^2}\sqrt{1-\frac{4m_l^2}{q^2}}\left(1+\frac{2m_l^2}{q^2}\right)\left(1-\frac{q^2}{m_{\eta'}^2}\right)^3 |F(q^2)|^2 \\ &= [\mathrm{QED}(q^2)] \times |F(q^2)|^2, \end{aligned} \quad (1)$$

where $m_{\eta'}$ and m_l are the masses of the η' meson and the lepton, respectively; α is the fine structure constant; and $[\mathrm{QED}(q^2)]$ represents the calculable QED part for a point-like meson. The TFF, $F(q^2)$, which is described by phenomenological models, can be experimentally determined from differences between the measured di-lepton invariant mass spectrum and the QED calculation. In the Vector Meson Dominance (VMD) model [5], it is assumed that interactions between virtual photon and hadrons are dominated by a superposition of neutral vector meson states. One commonly used expression for the multi-pole form factor is [6]:

$$F(q^2) = N \sum_V \frac{g_{\eta'\gamma V}}{2g_{V\gamma}} \cdot \frac{m_V^2}{m_V^2 - q^2 - i\Gamma_V m_V}, \quad (2)$$

where N is a normalization constant ensuring that $F(0) = 1$; $V = \rho, \omega, \phi$; m_V, Γ_V are the masses and widths of these vector mesons; and $g_{\eta'\gamma V}$ and $g_{V\gamma}$ are the corresponding coupling constants.

The parameter to be experimentally determined is the slope of the form factor b, which is related to the effective virtual vector meson mass Λ by

$$b = \frac{dF}{dq^2}\Big|_{q^2=0} = \Lambda^{-2} \quad (3)$$

In experiments, the single-pole form factor is generally used to extract the slope of the form factor. For the case of the η', the pole is expected to lie within the kinematic boundaries of the decay. The square of the form factor is described by

$$|F(q^2)|^2 = \frac{\Lambda^2(\Lambda^2+\gamma^2)}{(\Lambda^2-q^2)^2+\Lambda^2\gamma^2} \quad (4)$$

where the parameters Λ and γ correspond to the mass and width of the Breit-Wigner shape for the effective contributing vector meson. To a first approximation, $\Lambda \approx M_\rho \approx 0.7$ GeV and $\gamma \approx \Gamma_\rho \approx 0.12$ GeV.

For the η' Dalitz decay, only the process $\eta' \to \gamma\mu^+\mu^-$ has been observed and the slope of the form factor was measured to be $b_{\eta'} = (1.7 \pm 0.4)$ GeV^{-2} [1, 7]. To date, the process $\eta' \to \gamma e^+ e^-$ has not been observed yet. The most stringent upper limit on the ratio of decay widths $\Gamma(\eta' \to \gamma e^+ e^-)/\Gamma(\eta' \to \gamma\gamma)$ is 4.1×10^{-2} at the 90% confidence level (CL) from the CLEO Collaboration [8], which is above the predicted value of $(2.06 \pm 0.02) \times 10^{-2}$ from the modified VMD model [9].

In the VMD model, the TFF slope is expected to be $b_{\eta'} = 1.45$ GeV^{-2} [10, 11], while for chiral perturbation theory it is $b_{\eta'} = 1.60$ GeV^{-2} [12]. A recent calculation based on a dispersion integral gives $b_{\eta'} = 1.53^{+0.15}_{-0.08}$ GeV^{-2} [13].

We report the first observation of the $\eta' \to \gamma e^+ e^-$ decay and the extraction of the TFF. The source of the η' mesons are radiative $J/\psi \to \gamma\eta'$ decays in a sample of 1.31 billion J/ψ events (2.25×10^8 events were taken in 2009 [14] and 1.09×10^9 in 2012) [15] collected by the BESIII [16] at the BEPCII e^+e^- collider. The $\eta' \to \gamma\gamma$ decay events in the same data sample are used for normalization.

II. THE BESIII EXPERIMENT AND MONTE CARLO SIMULATION

BEPCII is a double-ring multi-bunch e^+e^- collider running in the tau-charm energy region. The BESIII detector, described in detail in Ref. [16], has a geometrical acceptance of 93% of 4π solid angle. It consists of a drift chamber (MDC), a time-of-flight (TOF) system, and an electromagnetic calorimeter (EMC), all enclosed in a super-conducting solenoid with 1.0 T (0.9 T in 2012) magnetic field. The small-cell helium based MDC provides the tracking of charged particle and ionization energy loss (dE/dx) measurement. The single cell position

resolution is 130 μm and the transverse momentum resolution is 0.5% at 1 GeV/c. The TOF system for particle identification (PID) is made of plastic scintillators. It has 80 ps time resolution in the barrel, and 110 ps in the end caps. The EMC is made of 6240 CsI (Tl) crystals. The energy resolution is 2.5% in the barrel and 5% in the end caps for 1.0 GeV photons. Outside the solenoid, a muon chamber system made of 1272 m^2 resistive plate chambers detects muon tracks with momenta greater than 0.5 GeV/c.

The GEANT4-based [17] simulation software BOOST includes the description of geometry and material of the BESIII detector, the detector response and digitization models, and also tracks the detector running conditions and performance. A Monte Carlo (MC) simulated sample of 1.2 billion J/ψ inclusive decays is used to study potential backgrounds. The production of the J/ψ resonance is simulated by the MC event generator KKMC [18]; the known decay modes are generated by EVTGEN [19, 20] with branching fractions set at the world average values [21], while unknown decays are generated by LUNDCHARM [22]. The EVTGEN package is used to generate $J/\psi \to \gamma\eta'$, $\eta' \to \gamma e^+e^-$ and $\eta' \to \gamma\gamma$ events. The decay $J/\psi \to \gamma\eta'$ is generated with an angular distribution of $1 + \cos^2\theta_\gamma$, where θ_γ is the radiative photon angle relative to the positron beam direction in the J/ψ rest frame. In generating $\eta' \to \gamma e^+e^-$, the TFF is parameterized by the multi-pole VMD model in Eq.(2) with the parameters taken from Ref. [1].

III. SIGNAL SELECTION: $J/\psi \to \gamma\eta', \eta' \to \gamma e^+e^-$

Charged tracks are reconstructed from hits registered in the MDC. Only tracks with $|\cos\theta| < 0.93$ are retained, where θ is the polar angle with respect to the beam axis. The tracks are required to pass within 10 cm of the center of the interaction region in the beam direction (Z axis) and within 1 cm in the plane perpendicular to the beam. Event candidates are required to have two well reconstructed charged tracks with net charge zero. For electron identification, information from dE/dx and TOF is combined to compute probabilities for the electron (Prob(e)) and pion (Prob(π)) hypothesis. To separate electrons from pions, we require Prob(e)/(Prob(e) + Prob(π)) > 0.95. Final states with kaons cannot contribute to the background because of the limited phase space.

Electromagnetic showers are reconstructed from clusters of energy deposits in the EMC. The photon candidate showers must have a minimum energy of 25 MeV in the barrel region ($|\cos\theta| < 0.80$) and 50 MeV in the end cap region ($0.86 < |\cos\theta| < 0.92$). Showers in the region between the barrel and the end caps are poorly measured and excluded from the analysis. To exclude charged-particle induced activities, the showers are required to be separated from the extrapolated positions of any charged track by at least 10°. In addition, cluster timing requirements are used to suppress electronic noise and unrelated energy deposits.

A vertex fit is performed on the electron and positron tracks, and a loose χ^2 requirement is applied to ensure that they come from a common vertex. To improve resolution and reduce background, a four-constraint (4C) kinematic fit is performed to the $\gamma\gamma e^+e^-$ hypothesis that constrains the total four-momentum of the detected particles to be equal to the initial four-momentum of the colliding beams. For events with more than two photon candidates, the combination with the smallest $\chi^2_{\rm 4C}$ is selected. Only events with $\chi^2_{\rm 4C}$ <100 are retained.

For the $J/\psi \to \gamma\eta', \eta' \to \gamma e^+e^-$ signal channel, the largest background comes from QED processes and $J/\psi \to e^+e^-\gamma\gamma$ decays. For these channels, the combination of the e^+e^- with any final-state photon produces a smooth $M(\gamma e^+e^-)$ distribution. The QED background mainly comes from $e^+e^- \to e^+e^-\gamma\gamma$ and $e^+e^- \to 3\gamma$ events in which one γ converts into an e^+e^- pair. These are studied using a e^+e^- collision data sample of 2.92 fb^{-1} taken at $\sqrt{s} = 3.773$ GeV [23], which is dominated by QED processes. For those processes, most of the photons have low energy and are at small angles relative to the incoming electron or positron beam directions. To reduce this background, the energy of the low-energy photon is further required to be higher than 200 MeV, and the angle between the photon and the electron or positron initial direction in the final states is required to be larger than 10°.

The primary peaking background comes from the decay $J/\psi \to \gamma\eta', \eta' \to \gamma\gamma$ followed by a γ conversion in the material in front of the MDC, including the beam pipe and the inner wall of the MDC. The distance from the reconstructed vertex point of the electron-positron pair to the z axis, defined as $\delta_{xy} = \sqrt{R_x^2 + R_y^2}$, is used to distinguish γ conversion events from signal events [24], where R_x and R_y are the distances in the x and y directions, respectively. A scatter plot of R_y versus R_x is shown in Fig. 1 (a) for MC-simulated $J/\psi \to \gamma\eta', \eta' \to \gamma\gamma$ decays, in which one of the photons undergoes conversion to an e^+e^- pair. As indicated in Fig. 1 (a), the inner circle matches the position of the beam pipe, while the outer circle corresponds to the position of the inner wall of the MDC. Figure 1 (b) shows the δ_{xy} distributions for the MC simulated $J/\psi \to \gamma\eta', \eta' \to \gamma e^+e^-$, $J/\psi \to \gamma\eta', \eta' \to \gamma\gamma$ events, together with the selected data events and events from the η' mass sideband. The two peaks above 2.0 cm correspond to the photon conversion of the γ from $J/\psi \to \gamma\eta', \eta' \to \gamma\gamma$ events, while the events near $\delta_{xy} = 0$ cm originate from the interaction point. We require $\delta_{xy} < 2$ cm to suppress the photon-conversion background, which retains about 80% of the signal events while removing about 98% of the photon-conversion events. After all selections, the normalized number of expected peaking background events from $J/\psi \to \gamma\eta', \eta' \to \gamma\gamma$ is 42.7 ± 8.0, where the error is dominantly from the difference in selection efficiencies

for the γ conversion events between data and MC.

Another possible source of peaking background is $J/\psi \to \gamma\eta', \eta' \to \gamma\pi^+\pi^-$, where the two pions are misidentified as an e^+e^- pair. The momenta of these pions are most below 200 MeV/c. An exclusive MC sample that includes coherent contributions from ρ, ω, and the box anomaly in the decay $\eta' \to \gamma\pi^+\pi^-$ [25] is used to study this background. We find that the kinematic fit to the electron-positron hypothesis shifts the spectrum away from the η' mass and, thus, the resulting M(γe^+e^-) distribution does not peak at the η' mass value. The normalized number of events from this background source after all selections is 9.7 ± 0.4, which is negligible compared to the non-peaking background from $e^+e^- \to e^+e^-\gamma\gamma$.

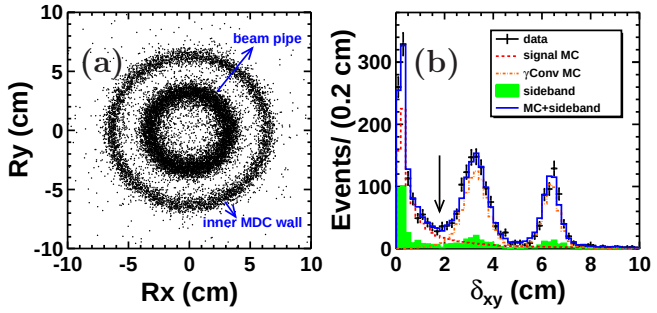

Figure 1. Electron-positron vertex position distribution: (a) scatter plot of R_y versus R_x for MC-simulated $J/\psi \to \gamma\eta'$, $\eta' \to \gamma\gamma$ events. (b) δ_{xy} distributions. The (black) crosses are data. The (red) dashed line shows the MC-simulated $J/\psi \to \gamma\eta'$, $\eta' \to \gamma e^+e^-$ signal events. The (orange) dotted-dashed histogram shows the background from γ-conversion events. The (green) shaded area is estimated from the η' mass sideband. The (blue) line is the sum of MC and the sideband estimate. In (b), the solid arrow indicates the requirement on δ_{xy}.

The combination of γe^+e^- with invariant mass closest to $m_{\eta'}$ is taken to reconstruct the η'. The resulting $M(\gamma e^+e^-)$ distribution after the selection criteria is shown in Fig. 2 and exhibits a clear peak at the η' mass. An unbinned extended maximum likelihood (ML) fit is performed to determine the signal yield. The signal probability density function (PDF) is represented by the signal MC shape. The shape for the non-peaking background is described by a first-order Chebychev polynomial. The background yield and its PDF parameters are allowed to vary in the fit. The peaking background from the γ-conversion of $J/\psi \to \gamma\eta', \eta' \to \gamma\gamma$ decay is obtained from the MC-simulated shape with the yield fixed as described before. The fitting range is $0.85-1.05$ GeV/c^2. The net signal yield and the detection efficiency are summarized in Table I.

Table I. Number of observed signal events, $N_{\eta' \to \gamma e^+e^-}$ ($N_{\eta' \to \gamma\gamma}$), and detection efficiency, $\epsilon_{\eta' \to \gamma e^+e^-}$ ($\epsilon_{\eta' \to \gamma\gamma}$) for $J/\psi \to \gamma\eta', \eta' \to \gamma e^+e^-$ ($J/\psi \to \gamma\eta', \eta' \to \gamma\gamma$). The uncertainties are statistical only.

	$\eta' \to \gamma e^+e^-$	$\eta' \to \gamma\gamma$
$N_{\eta' \to \gamma e^+e^-}$ ($N_{\eta' \to \gamma\gamma}$)	864 ± 36	70846 ± 292
$\epsilon_{\eta' \to \gamma e^+e^-}$ ($\epsilon_{\eta' \to \gamma\gamma}$)	24.5%	42.8%

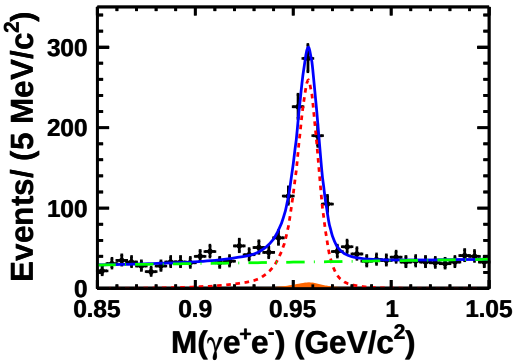

Figure 2. Invariant γe^+e^- mass distribution for the selected signal events. The (black) crosses are the data, the (red) dashed line represents the signal, the (green) dot-dashed curve shows the non-peaking background shapes, the (orange) shaded component is the shape of the $J/\psi \to \gamma\eta', \eta' \to \gamma\gamma$ peaking background events. The total fit result is shown as the (blue) solid line.

IV. NORMALIZATION CHANNEL: $J/\psi \to \gamma\eta', \eta' \to \gamma\gamma$

The decay $J/\psi \to \gamma\eta', \eta' \to \gamma\gamma$ is studied using the same data set, and we quote our result in terms of the ratio $\Gamma(\eta' \to \gamma e^+e^-)/\Gamma(\eta' \to \gamma\gamma)$. In this ratio the uncertainties due to the total number of J/ψ events and the branching fraction for $J/\psi \to \gamma\eta'$ cancel, and the uncertainty due to the photon detection efficiency partially cancels.

Events with zero charged particles and at least three photon candidates are selected with the same requirements that are used for the signal events. A 4C kinematic fit is performed to the $J/\psi \to \gamma\gamma\gamma$ hypothesis. For events with more than three photons, the combination with the smallest χ^2_{4C} is selected. The χ^2_{4C} is required to be less than 100. The two photon combination with invariant mass $M(\gamma\gamma)$ closest to $m_{\eta'}$ is taken as from the η' decay.

Detailed MC studies indicate that no peaking background remains after all the selection criteria. The non-peaking background mainly comes from the continuum process $e^+e^- \to \gamma\gamma\gamma$ and $J/\psi \to \gamma\pi^0\pi^0$ decays. The latter source involves intermediate states such as the

$f_0(1500), f_0(1710), f_0(2020), f_2(1270), f_4(2050)$. Because the η' decays isotropically, the angular distribution of photons from the η' decays is flat in $\cos\theta_{\rm decay}$, where $\theta_{\rm decay}$ is the angle of the decay photon in the η' helicity frame. In contrast, background events from QED continuum processes and $J/\psi \to \gamma\pi^0\pi^0$ decays tend to accumulate near $\cos\theta_{\rm decay} = \pm 1$. We suppress these non-peaking backgrounds by requiring $|\cos\theta_{\rm decay}| < 0.8$.

The $M(\gamma\gamma)$ distribution for events that survive the selection requirements is shown in Fig. 3. An unbinned ML fit is performed to obtain the yield of $J/\psi \to \gamma\eta', \eta' \to \gamma\gamma$. The PDF used to represent the signal is taken from the MC, and the PDF for the non-peaking background is a first-order Chebychev polynomial with coefficients determined from the fit. The resulting signal yield and the MC-determined detection efficiency are summarized in Table I.

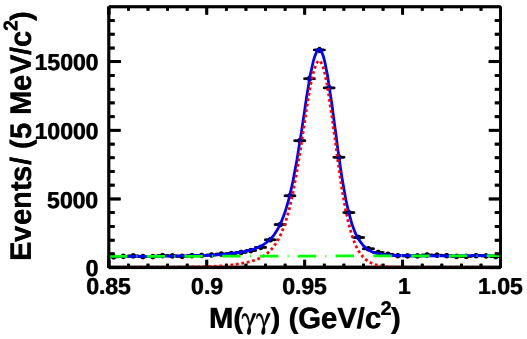

Figure 3. Invariant mass distribution of $M(\gamma\gamma)$ for the selected events in the normalization channel. The (black) crosses are data, the (red) dashed curves represents the $\eta' \to \gamma\gamma$ signal, the (green) dot-dashed curve shows the non-peaking background. The fit result is shown as the (blue) solid curve.

V. SYSTEMATIC UNCERTAINTIES IN THE RELATIVE DECAY WIDTH

Table II lists all sources of systematic uncertainties associated with the measurement of the ratio $\Gamma(\eta' \to \gamma e^+e^-)/\Gamma(\eta' \to \gamma\gamma)$. Most systematic uncertainties are determined from comparisons of low-background, high-statistics data samples with results from MC simulations.

The electron and positron tracking and PID efficiencies are determined using a sample of radiative Bhabha $e^+e^- \to \gamma e^+e^-$ (including $J/\psi \to \gamma e^+e^-$) events collected at the J/ψ energy. Differences in tracking and PID efficiencies between data and MC simulation are determined for every bin of a two-dimensional distribution of the momentum versus polar angle of the lepton tracks. These are used to determine an overall weighted difference per track of $(1.1 \pm 0.3)\%$ for the tracking efficiency and $(1.9 \pm 0.3)\%$ for the PID efficiency. The MC efficiency is corrected for these differences, and the uncertainties of the correction coefficients are assigned as the systematic uncertainties associated with the lepton tracking and PID efficiencies.

Table II. Summary of relative systematic uncertainties for the determination of the ratio $\frac{\Gamma(\eta' \to \gamma e^+e^-)}{\Gamma(\eta' \to \gamma\gamma)}$. The last row is the uncertainty associated with the $J/\psi \to \gamma\eta', \eta' \to \gamma\gamma$ normalization sample.

Sources	Systematic uncertainties(in %)
MDC tracking	0.6
PID	0.6
Photon detection	1.0
Veto of gamma conversion	1.8
4C kinematic fit	1.0
Form factor uncertainty	1.6
Fit range & Bkg shape	0.9
Uncertainty of $N_{\eta' \to \gamma\gamma}$	1.2
Total	3.3

The systematic uncertainty associated with the photon detection efficiency is studied using three different methods, as described in Ref. [26]. The three methods provide consistent results for the photon efficiency uncertainty to be 1% per photon. Because the systematic uncertainty from the radiative photon and one photon from the η' cancel in the ratio, the total systematic uncertainty from photon detection is 1%.

In the analysis, the peaking background from $J/\psi \to \gamma\eta', \eta' \to \gamma\gamma$ γ-conversion events is suppressed by the requirement $\delta_{xy} < 2$ cm. To estimate the systematic uncertainty associated with this requirement, we use a sample of $J/\psi \to \pi^+\pi^-\pi^0, \pi^0 \to \gamma e^+e^-$ that includes both π^0 Dalitz decays and $\pi^0 \to \gamma\gamma$ decays with one photon externally converted to an electron-positron pair. The data-MC difference of 1.8% for these events is considered as the systematic uncertainty for our γ-conversion veto requirement on δ_{xy}.

A systematic uncertainty associated with the kinematic fit will occur if the track-helix parameters for data and MC simulated events are not consistent. Following the procedure described in Ref. [27], we use the $J/\psi \to \pi^+\pi^-\pi^0, \pi^0 \to \gamma e^+e^-$ decay as a control sample to extract the correction factors from the pull distributions of the track helix parameters. The 1% difference between the efficiencies with and without helix parameter corrections is taken as the systematic uncertainty.

To estimate the systematic uncertainty due to the efficiency dependence on the choice of form-factor parameterizations, signal MC events are also generated using a single-pole VMD model, shown in Eq. (4), with $\Lambda = (0.79 \pm 0.05)$ GeV and $\gamma = (0.13 \pm 0.06)$ GeV, which

are taken from the fitted results described below in Section VII. The relative difference in the detection efficiency compared to that of the multi-pole model is taken as the uncertainty associated with the form-factor parameterization.

In the fit to the γe^+e^- mass distribution, the signal PDF is fixed to the signal MC shape. An alternative fit is performed by using a convolution of a MC signal shape with a Gaussian function that is used to describe the MC-data difference due to the resolution. The fitted width of the Gaussian is (0.39 ± 0.19) MeV, and the fit yields 863.8 ± 36.0 signal events. The difference from the nominal fit is negligible. Finally, the uncertainty due to the non-peaking background shape is estimated by varying the PDF shape and fitting range in the ML fit. The changes in yields for these variations give systematic uncertainties due to these backgrounds.

The systematic uncertainty in the measurement of $J/\psi \to \gamma\eta', \eta' \to \gamma\gamma$ associated with the uncertainty from the kinematic fit is estimated using a control sample of $e^+e^- \to \gamma\gamma\gamma$ at 3.650 GeV [28] and found to be less than 1%. The uncertainty for this channel due to background is estimated to be less than 0.3% from variations in the PDF shape and fitting range. The uncertainty from the requirement $|\cos\theta_{\rm decay}| < 0.8$ is 0.4%. When combined with the 0.4% statistical uncertainty, the total uncertainty associated with $N_{\eta'\to\gamma\gamma}$ is 1.2%.

Assuming all systematic uncertainties in Table II are independent, the total systematic uncertainty, obtained from their quadratic sum, is 3.3%.

VI. RELATIVE DECAY WIDTH

The ratio $\Gamma(\eta' \to \gamma e^+e^-)/\Gamma(\eta' \to \gamma\gamma)$ is determined using the following formula:

$$\frac{\Gamma(\eta' \to \gamma e^+e^-)}{\Gamma(\eta' \to \gamma\gamma)} = \frac{N_{\eta'\to\gamma e^+e^-}}{N_{\eta'\to\gamma\gamma}} \cdot \frac{\epsilon_{\eta'\to\gamma\gamma}}{\epsilon_{\eta'\to\gamma e^+e^-}}, \quad (5)$$

where $N_{\eta'\to\gamma e^+e^-}$ ($N_{\eta'\to\gamma\gamma}$) and $\epsilon_{\eta'\to\gamma e^+e^-}$ ($\epsilon_{\eta'\to\gamma\gamma}$) are the number of observed signal events and the detection efficiency, respectively, for $J/\psi \to \gamma\eta', \eta' \to \gamma e^+e^-$ ($J/\psi \to \gamma\eta', \eta' \to \gamma\gamma$) decays, as listed in Table I. The result is

$$\frac{\Gamma(\eta' \to \gamma e^+e^-)}{\Gamma(\eta' \to \gamma\gamma)} = (2.13 \pm 0.09(\text{stat.}) \pm 0.07(\text{sys.})) \times 10^{-2}. \quad (6)$$

Using the $\eta' \to \gamma\gamma$ branching fraction value listed in PDG [21], we obtain the first measurement of the $\eta' \to \gamma e^+e^-$ branching fraction of

$$\mathcal{B}(\eta' \to \gamma e^+e^-) = (4.69 \pm 0.20(\text{stat.}) \pm 0.23(\text{sys.})) \times 10^{-4}. \quad (7)$$

VII. FORM FACTOR MEASUREMENT

The TFF is extracted from the bin-by-bin efficiency corrected signal yields for eight different $M(e^+e^-)$ bins. The bin widths are all chosen to be 0.1 GeV/c^2. Since this is much wider than the $M(e^+e^-)$ resolution, which is 5∼6 MeV/c^2 depending on $M(e^+e^-)$, no unfolding is needed. The signal yield in each $M(e^+e^-)$ bin i is obtained by performing bin-by-bin fits to the $M(\gamma e^+e^-)$ mass distributions using the fitting procedure described in Section III. The peaking background from the $J/\psi \to \gamma\eta', \eta' \to \gamma\gamma$ only exists in the first bin, and the yield is fixed to the normalized number in the bin. The fit results are shown in Fig. 4. The fitted ($n_i^{\rm obs}$) and efficiency-corrected signal yields ($n_i^{\rm corr}$) for each $M_i(e^+e^-)$ bin are summarized in Table III. Figure 5 shows the efficiency-corrected signal yields versus $M(e^+e^-)$ with the QED shape superimposed for comparison. The discrepancy between QED and data, which reflects the TFF, is evident in the high $M(e^+e^-)$ region.

The systematic uncertainties on $n_i^{\rm corr}$ include the uncertainty from the MDC tracking efficiency, PID, photon detection, kinematic fit, veto of gamma conversion, background description and signal shape; they are the same as those described in Section V.

The partial ratio $r_i = \Delta\Gamma(\eta' \to \gamma e^+e^-)_i/\Gamma(\eta' \to \gamma\gamma)$ for each given $M(e^+e^-)$ bin i, is defined as

$$r_i \equiv \frac{\Delta\Gamma(\eta' \to \gamma e^+e^-)_i}{\Gamma(\eta' \to \gamma\gamma)} = \frac{n_i^{\rm corr}\epsilon_{\eta'\to\gamma\gamma}}{N_{\eta'\to\gamma\gamma}}, \quad (8)$$

where $\Delta\Gamma(\eta' \to \gamma e^+e^-)_i$ is the integrated rate in each $M(e^+e^-)$ interval.

The result for $|F|^2$ in each $M(e^+e^-)$ bin is obtained by dividing the value r_i by the integrated QED predication in each $M(e^+e^-)$ interval (see Eq. (1)). The values of $|F|^2$ for each $M(e^+e^-)$ bin are summarized in Table IV.

A variety of models have been traditionally used to parameterize the TFF. The most common one, based on VMD [5], uses only the first term in the dispersion relation. In this single pole model, the TFF is given by Eq. (4). The results of a least-squares fit with the single pole model is shown in Fig. 6; the parameters of the form factors are determined to be $\Lambda_{\eta'} = (0.79 \pm 0.05)$ GeV, $\gamma_{\eta'} = (0.13 \pm 0.06)$ GeV. From the fitted value of the parameter $\Lambda_{\eta'}$, the slope of the form factor is obtained to be (1.60 ± 0.19) GeV^{-2}, in agreement with the result $b_{\eta'} = (1.7 \pm 0.4)$ GeV^{-2} obtained in the process of $\eta' \to \gamma\mu^+\mu^-$ [1].

To test the robustness of the slope extracted from the simple pole model, we also fit the data below 0.5 GeV/c^2 using the single pole Ansatz used in lighter meson studies:

$$F(q^2) = \frac{1}{(1 - q^2/\Lambda^2)}, \quad (9)$$

The parameterization diverges at $M(e^+e^-) = \Lambda$ and, therefore, can not be used for the whole kinematic region. The result of this fit is shown in Fig. 7. The slope of the

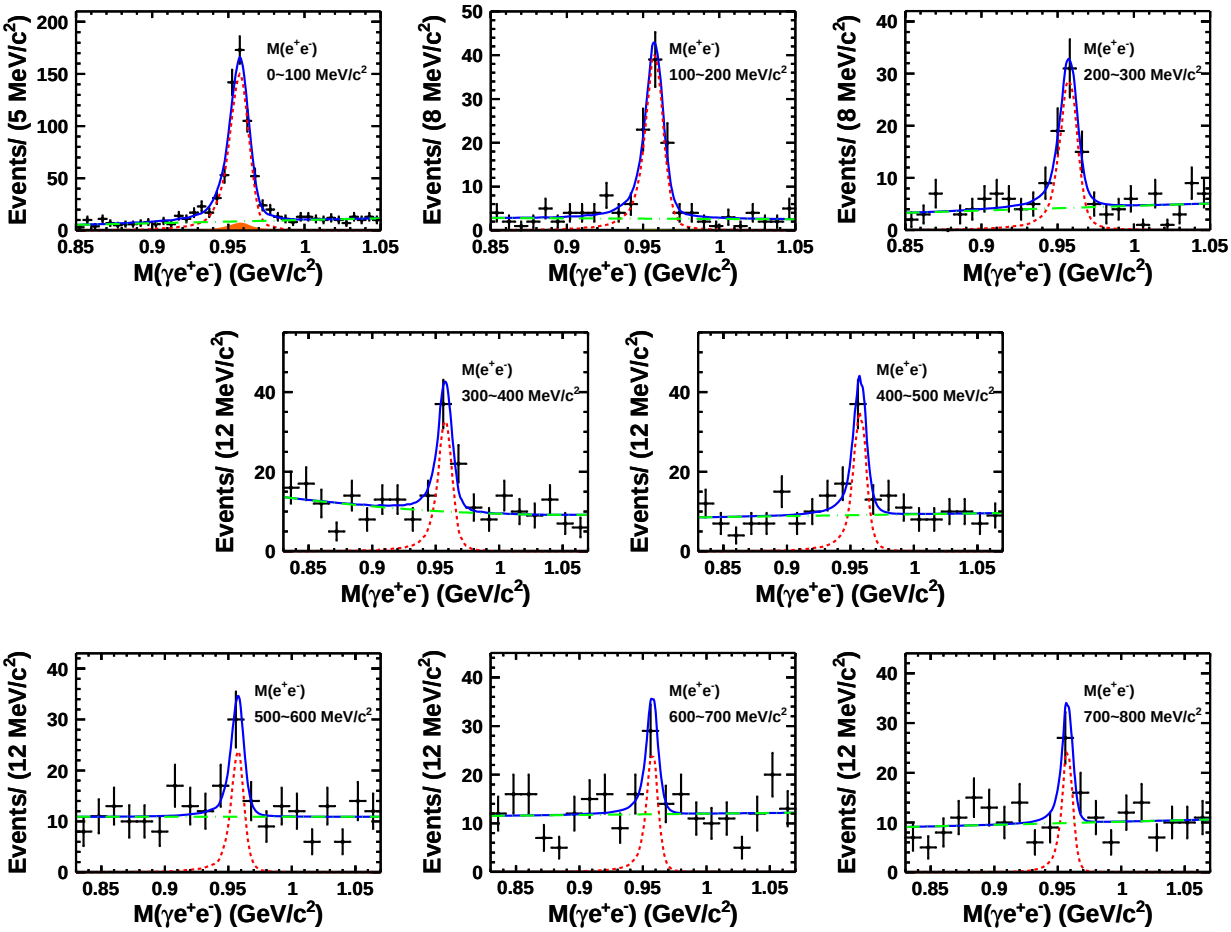

Figure 4. Results from bin-by-bin fits to the $M(\gamma e^+e^-)$ distributions for different $M(e^+e^-)$ bins. The (black) crosses are data, the (red) dashed curves represent the signal, the (green) dot-dashed curves show the non-peaking backgrounds, the (orange) shaded component for the $M(e^+e^-) < 100$ MeV/c^2bin is the shape of the peaking background from $J/\psi \to \gamma\eta', \eta' \to \gamma\gamma$. The total fit results are shown as (blue) solid curves.

Table III. Fitted ($n_i^{\rm obs}$) and efficiency-corrected ($n_i^{\rm corr}$) signal yields for the eight $M(e^+e^-)$ bins, and ratios (r_i). The uncertainties are statistical only.

$M(e^+e^-)$ (GeV/c^2)	[0.0, 0.1]	[0.1, 0.2]	[0.2, 0.3]	[0.3, 0.4]
$n_i^{\rm obs}$	545 ± 27	86.5 ± 10.7	62.1 ± 9.8	45.6 ± 9.7
$n_i^{\rm corr}$	2380 ± 120	368 ± 46	194 ± 31	128 ± 27
r_i (10^{-2})	1.44 ± 0.07	0.22 ± 0.03	0.12 ± 0.02	0.08 ± 0.02
$M(e^+e^-)$ (GeV/c^2)	[0.4, 0.5]	[0.5, 0.6]	[0.6, 0.7]	[0.7, 0.8]
$n_i^{\rm obs}$	45.4 ± 9.0	29.9 ± 8.0	28.0 ± 7.8	25.0 ± 6.9
$n_i^{\rm corr}$	135 ± 27	93.3 ± 25.0	96.2 ± 26.8	109 ± 30
r_i (10^{-2})	0.08 ± 0.02	0.06 ± 0.02	0.06 ± 0.02	0.07 ± 0.02

Table IV. Values of $|F|^2$ in each $M(e^+e^-)$ bin, where the first uncertainties are statistical and the second ones systematic.

$M(e^+e^-)$ (GeV/c^2)	[0.0, 0.1]	[0.1, 0.2]	[0.2, 0.3]	[0.3, 0.4]
$\|F\|^2$	$1.05 \pm 0.05 \pm 0.03$	$1.12 \pm 0.14 \pm 0.04$	$1.16 \pm 0.18 \pm 0.05$	$1.33 \pm 0.28 \pm 0.05$
$M(e^+e^-)$ (GeV/c^2)	[0.4, 0.5]	[0.5, 0.6]	[0.6, 0.7]	[0.7, 0.8]
$\|F\|^2$	$2.48 \pm 0.49 \pm 0.25$	$3.30 \pm 0.88 \pm 0.31$	$7.66 \pm 2.13 \pm 0.89$	$26.6 \pm 7.3 \pm 1.9$

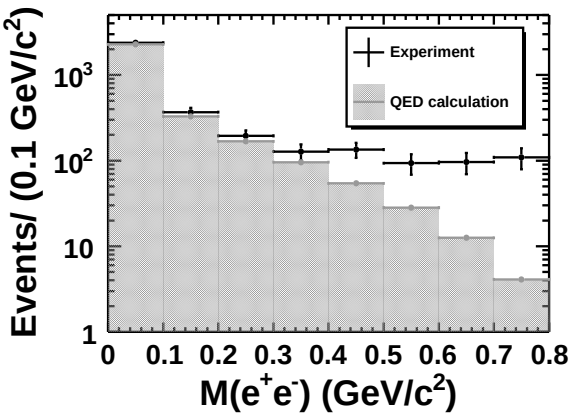

Figure 5. Efficiency-corrected signal yields $n_i^{\rm corr}$ versus $M(e^+e^-)$. The (black) crosses are data and the (gray) shaded histogram indicates the point-like QED result.

form factor is determined to be $b_{\eta'} = (1.58 \pm 0.34)$ GeV^{-2}, which is in good agreement with the result of (1.60 ± 0.19) GeV^{-2} using Eq. (4).

The quadratic difference between the uncertainties of the parameters with only statistical errors used in the fits and the uncertainties of the parameters with combined statistical and systematic errors used in the fits is taken as the systematic uncertainty on the parameters. The resulting parameters in Eq. (4) are determined to be $\Lambda_{\eta'} = (0.79 \pm 0.04(\text{stat.}) \pm 0.02(\text{sys.}))$ GeV, $\gamma_{\eta'} = (0.13 \pm 0.06(\text{stat.}) \pm 0.03(\text{sys.}))$ GeV, respectively.

VIII. SUMMARY

In summary, with a sample of 1.31 billion J/ψ events collected in the BESIII detector, we have made the first measurement of the EM Dalitz decay process $\eta' \to \gamma e^+e^-$ and measure the ratio $\Gamma(\eta' \to \gamma e^+e^-)/\Gamma(\eta' \to \gamma\gamma) = (2.13 \pm 0.09(\text{stat.}) \pm 0.07(\text{sys.})) \times 10^{-2}$. Using the PDG value for the $\eta' \to \gamma\gamma$ branching fraction [21], we determine $\mathcal{B}(\eta' \to \gamma e^+e^-) = (4.69 \pm 0.20(\text{stat.}) \pm 0.23(\text{sys.})) \times 10^{-4}$. We present measurements of the TFF as a function of $M(e^+e^-)$. Our TFF results can be described with a single pole parameterization Eq. (4), with mass and width parameters of $\Lambda_{\eta'} = (0.79 \pm 0.04(\text{stat.}) \pm 0.02(\text{sys.}))$ GeV, and $\gamma_{\eta'} = (0.13 \pm 0.06(\text{stat.}) \pm 0.03(\text{sys.}))$ GeV, respectively. The slope of the TFF corresponds to $(1.60 \pm 0.17(\text{stat.}) \pm 0.08(\text{sys.}))$ GeV^{-2} and agrees within errors with the VMD model predictions. The uncertainty of the η' transition form factor slope matches the best determination in the space-like region from the CELLO collaboration $b_{\eta'} = (1.60 \pm 0.16)$ GeV^{-2} [29], and improves the previous determination of the slope in the time-like region $b_{\eta'} = (1.7 \pm 0.4)$ GeV^{-2} [1, 7]. The η' form factor is determined by both universal $\pi^+\pi^-$ rescattering and a reaction specific part, with the latter contributing about 20% to the form factor slope [13]. Therefore our result is sensitive specifically to the η' internal EM structure. In addition, the decay $\eta' \to \gamma e^+e^-$ is closely related to $\eta' \to \gamma\pi^+\pi^-$, and in particular the transition form factor could be predicted from the invariant mass distribution of the two pions and the branching ratio of the $\eta' \to \gamma\pi^+\pi^-$ decay in a model independent way using a dispersive integral. Also, the knowledge of the TFF is useful for studies of the HLbL scattering contribution to the muon anomalous magnetic moment, $a_\mu = (g_\mu - 2)/2$ [4].

IX. ACKNOWLEDGMENT

The BESIII collaboration thanks the staff of BEPCII and the IHEP computing center for their strong support. This work is supported in part by National Key Basic Research Program of China under Contract No. 2015CB856700; National Natural Science Foundation of China (NSFC) under Contracts Nos. 11125525, 11235011, 11322544, 11335008, 11425524; the Chinese Academy of Sciences (CAS) Large-Scale Scientific Facility Program; Joint Large-Scale Scientific Facility Funds of the NSFC and CAS under Contracts Nos. 11179007, U1232201, U1332201; CAS under Contracts Nos. KJCX2-YW-N29, KJCX2-YW-N45; 100 Talents Program of CAS; INPAC and Shanghai Key Laboratory for Particle Physics and Cosmology; German Research Foundation DFG under Contract No. Collaborative Research Center CRC-1044; Istituto Nazionale di Fisica Nucleare, Italy; Ministry of Development of Turkey under Contract No. DPT2006K-120470; Russian Foundation for Basic Research under Contract No. 14-

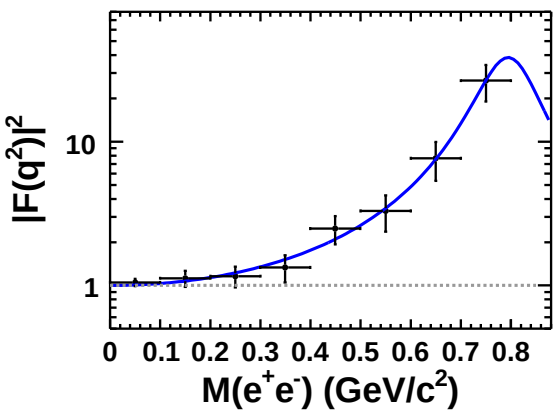

Figure 6. Fit to the single pole form factor $|F|^2$ using Eq. (4). The (black) crosses are data, where the statistical and systematic uncertainties are combined, the (blue) solid curve shows the fit results. The (gray) dotted line shows to the point-like case (*i.e.* with $|F|^2 = 1$) for comparison.

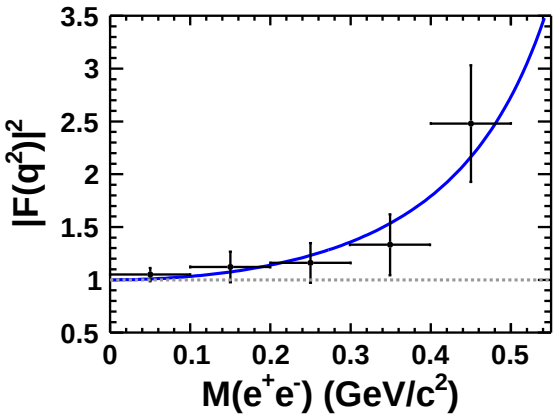

Figure 7. Determination of the form factor slope by fitting to $|F|^2$ using the single pole form factor of Eq. (9). The (black) crosses are data, where the uncertainties are the combined statistical and systematic uncertainties, the (blue) solid curve shows the fit result. The (gray) dotted line corresponds to the point-like particle case (with $|F|^2 = 1$).

07-91152; U. S. Department of Energy under Contracts Nos. DE-FG02-04ER41291, DE-FG02-05ER41374, DE-FG02-94ER40823, DESC0010118; U.S. National Science Foundation; University of Groningen (RuG) and the Helmholtzzentrum fuer Schwerionenforschung GmbH (GSI), Darmstadt; WCU Program of National Research Foundation of Korea under Contract No. R32-2008-000-10155-0

[1] L. G. Landsberg, Phys. Rept. **128**, 301 (1985).
[2] N. M. Kroll and W. Wada, Phys. Rev. **98**, 1355 (1955).
[3] E. Czerwinski, S. Eidelman, C. Hanhart, B. Kubis, A. Kupsc, S. Leupold, P. Moskal, S. Schadmand, arXiv:1207.6556 [hep-ph].
[4] T. Blum, A. Denig, I. Logashenko, E. de Rafael, B. Lee Roberts, T. Teubner and G. Venanzoni, arXiv:1311.2198 [hep-ph].
[5] J. J. Sakurai, Currents and Mesons, Ann. of Physics, 11 (1960).
[6] V. M. Budnev and V. A. Karnakov, Pisma Zh. Eksp. Teor. Fiz. **29**, 439 (1979).
[7] R. I. Dzhelyadin, S. V. Golovkin, M. V. Gritsuk, V. A. Kachanov, D. B. Kakauridze, A. S. Konstantinov, V. F. Konstantinov and V. P. Kubarovsky *et al.*, Phys. Lett. B **88**, 379 (1979) [JETP Lett. **30**, 359 (1979)].
[8] R. A. Briere *et al.* (CLEO Collaboration), Phys. Rev. Lett. **84**, 26 (2000).
[9] T. Petri, arXiv:1010.2378 [nucl-th].
[10] A. Bramon, E. Masso, Phys. Lett. B **104**, 311 (1981).
[11] L. Ametller, L. Bergstrom, A. Bramon, E. Masso, Nucl. Phys. B **228**, 301 (1983).
[12] L. Ametller, J. Bijnens, A. Bramon, F. Cornet, Phys. Rev. D **45**, 986 (1992).
[13] C. Hanhart, A. Kupsc, U. G. Meiner, F. Stollenwerk, and A. Wirzba, Eur. Phys. J. C **73**, 2668 (2013)
[14] M. Ablikim *et al.* (BESIII Collaboration), Chinese Phys. C **36**, 915 (2012).
[15] With the same approach as for J/ψ events taken in 2009 (see Ref. [14] for more details), the preliminary number

of J/ψ events taken in 2009 and 2012 is determined to be 1310.6×10^6 with an uncertainty of 0.8%.
[16] M. Ablikim *et al.* (BESIII Collaboration), Nucl. Instrum. Meth. A **614**, 345 (2010).
[17] S. Agostinelli *et al.* (GEANT4 Collaboration), Nucl. Instrum. Meth. A **506**, 250 (2003).
[18] S. Jadach, B.F.L. Ward, and Z. Was, Comput. Phys. Commun. **130**, 260 (2000); Phys. Rev. D **63**, 113009 (2001).
[19] D. J. Lange, Nucl. Instrum. Meth. A **462**, 152 (2001).
[20] R. G. Ping, Chinese Phys. C **32**, 599 (2008).
[21] K. A. Olive et al. (Particle Data Group), Chinese Phys. C **38**, 090001 (2014).
[22] J. C. Chen, G. S. Huang, X. R. Qi, D. H. Zhang and Y. S. Zhu, Phys. Rev. D **62**, 034003 (2000).
[23] M. Ablikim *et al.* (BESIII Collaboration), Chinese Phys. C **37**, 123001 (2013).
[24] Z. R. Xu and K. L. He, Chinese Phys. C **36**, 742 (2012).
[25] M. Ablikim *et al.* (BESIII Collaboration), Phys. Rev. D **87**, 092011 (2013).
[26] M. Ablikim *et al.* (BESIII Collaboration), Phys. Rev. D **83**, 112005 (2011).
[27] M. Ablikim *et al.* (BESIII Collaboration), Phys. Rev. D **87**, 012002 (2013).
[28] M. Ablikim *et al.* (BESIII Collaboration), Phys. Rev. D **85**, 112008 (2012).
[29] H. J. Behrend *et al.* (CELLO Collaboration), Z. Phys. C **49**, 401 (1991).